INTERNATIONAL JOURNAL FOR NUMERICAL METHODS IN FLUIDS
Int. J. Numer. Meth. Fluids **28**: 859–881 (1998)

VISCOUS FLOW WITH LARGE FLUID–FLUID INTERFACE DISPLACEMENT

HENRIK KOBLITZ RASMUSSEN[a], OLE HASSAGER[b] AND ARILD SAASEN[c,1]

[a] *Department of Manufacturing Engineering, Technical University of Denmark, DK-2800 Lyngby, Denmark*
[b] *Danish Polymer Centre, Department of Chemical Engineering, Technical University of Denmark, DK-2800 Lyngby, Denmark*
[c] *Department of Petroleum Technology, Rogaland University Centre, PO Box 2557, Ullandhaug, N-4004 Stavanger, Norway*

SUMMARY

The arbitrary Lagrange–Euler (ALE) kinematic description has been implemented in a 3D transient finite element program to simulate multiple fluid flows with fluid–fluid interface or surface displacements. The description of fluid interfaces includes variable interfacial tension, and the formulation is useful in the simulation of low and intermediate Reynolds number viscous flow. The displacement of two immiscible Newtonian fluids in a vertical (concentric and eccentric) annulus and a (vertical and inclined) tube is simulated. © 1998 John Wiley & Sons, Ltd.

KEY WORDS: 3D; finite elements; arbitrary Lagrange–Euler; fluid–fluid interfaces; annulus; displacement

1. INTRODUCTION

Displacement of one fluid by another is an important operation in the drilling of oil wells [1] and in connection with polymer processing operations such as injection moulding. Therefore, the objective is to develop and implement a 3D scheme for the numerical simulation of multiple fluid flows with fluid–fluid interface or surface displacement.

The two classic kinematic descriptions in fluid mechanics are the Lagrangian and the Eulerian. Both formulations present advantages and disadvantages as discussed by Huerta and Liu [2]. The Lagrangian description easily handles the free interface, but the observation point follows the fluid particle, which leads to element distortion. On the other hand, the fixed observation point in the Eulerian formulation presents a problem in situations with free interfaces. Hence, the arbitrary Lagrange–Euler (ALE) kinematic description, which represents a combination of the two methods [2–4], is used.

A general review of methods for simulation with the arbitrary Lagrange–Euler kinematic may be found elsewhere (see Reference [5]).

The use of an ALE formulation in itself, however, does not guarantee easy handling of large interfacial distortions. In fact, the applicability for the description of large distortions depends on the construction of the method, including the detailed technique for the mesh movement. In an earlier development [6] an ALE formulation was used with pure Lagrangian behaviour on the interface. In that technique the element nodes tend to accumulate in regions where they

---

[1] Present address: Statoil (den norske stats oljeselskap a.s.), N-4035 Stavanger, Norway.

CCC 0271–2091/98/150859–23$17.50

Received January 1997
Revised September 1997

are not needed. Consequently, in the present development, the node motion on the interface is controled with the use of a modification of the well-known spine technique [7].

2. MATHEMATICAL FORMULATION

The ALE method involves a moving domain of reference (mesh) as well as a moving fluid domain. In principle, the mesh is free to move in an arbitrary fashion in the interior of the fluid domain, but another situation exists on the boundary and on fluid–fluid interfaces. Here it is important that the two domains follow one another. In other words, although the interior nodes in the arbitrary Lagrange–Euler formulation are truly free to move arbitrarily, the boundary nodes must satisfy a condition that makes the boundaries of the reference domain and fluid domain coincide. A derivation of this condition is presented here. This condition has been given earlier (e.g. Reference [4]), but the present paper attempts to present an alternative derivation, motivated by the fact that the treatment, including discretization, of this condition is the key to the large interfacial deformations obtainable in the present method.

2.1. The material interface equation

The notation of Szabo and Hassager [5] is followed closely. In the following, the motion of an interface relative to an arbitrarily moving observation point, $\boldsymbol{x}(t) = (x_1(t), x_2(t), x_3(t))$ is considered.

$h(\boldsymbol{x}, t) = 0$ denotes a 2D surface or interface in the 3D flow domain, and $\boldsymbol{v} = \boldsymbol{v}(\boldsymbol{x}, t)$ denotes the velocity at position $\boldsymbol{x}$ and time t, respectively.

A requirement of the kinematic description of a free interface is that the interface is a material interface. The material interface equation at a given $\boldsymbol{x}$ and as a function of the time t is

$$\frac{\partial h}{\partial t} + v_i \frac{\partial h}{\partial x_i} = 0. \tag{1}$$

Consider a path ξ in space, given by

$$x_i = z_i(\xi, t), \tag{2}$$

where $z_i(\xi, t)$ gives the co-ordinates of the observation point as a function of time. The interface function h is denoted at the observation point $\bar{h}(\xi, t)$, so that

$$\bar{h}(\xi, t) = h(z_i(\xi, t), t). \tag{3}$$

Therefore, the material interface becomes

$$\left(\frac{\partial \bar{h}}{\partial t}\right) = \frac{\partial h}{\partial t} + \left(\frac{\partial h}{\partial x_i}\right)_{x_i = z_i} \left(\frac{\partial z_i}{\partial t}\right) = \frac{\partial h}{\partial t} + \left(\frac{\partial h}{\partial x_i}\right)_{x_i = z_i} w_i. \tag{4}$$

The components w_i of the velocity of the observation point are defined here.

The equation of the material interface referring to the moving observation point is then obtained by inserting Equation (4) into (1):

$$\left(\frac{\partial \bar{h}}{\partial t}\right) + (v_i - w_i)\left(\frac{\partial h}{\partial x_i}\right)_{x_i = z_i} = 0, \tag{5}$$

or, more concisely,

$$\left(\frac{\partial \bar{h}}{\partial t}\right) + (\boldsymbol{v} - \boldsymbol{w})\cdot(\boldsymbol{\nabla} h)_{x=z} = 0. \tag{6}$$

If $\boldsymbol{z}(\xi, t)$ follows the material interface, then

$$\frac{d\bar{h}}{dt} = 0. \tag{7}$$

Equation (6) is then stated

$$(\boldsymbol{v} - \boldsymbol{w})\cdot(\boldsymbol{\nabla} h)_{x=z} = 0. \tag{8}$$

If $\boldsymbol{n} = (\boldsymbol{n})_{x=z}$ denotes the outward vector normal to the surface (shown in Figure 1) then $(\boldsymbol{\nabla} h)_{x=z} = |(\boldsymbol{\nabla} h)_{x=z}|\boldsymbol{n}$. Hence,

$$(\boldsymbol{v} - \boldsymbol{w})\cdot\boldsymbol{n} = 0, \tag{9}$$

in accordance with Soulaimani *et al.* [4]. This is the equation needed in order to describe an interface in an ALE concept.

The equation defines w_i as

$$w_i(\xi, t) = \frac{\partial}{\partial t} z_i(\xi, t), \tag{10}$$

or, more concisely,

$$\boldsymbol{w} = \frac{\partial \boldsymbol{z}}{\partial t}. \tag{11}$$

2.2. The equation of motion and continuity

As in the derivation of the material interface equation, Szabo and Hassager [5] derived the equation of continuity and motion referring to a moving observation point with co-ordinates $z_i(\xi, t)$ on the path ξ.

The equation of continuity becomes

$$(\boldsymbol{\nabla}\cdot\boldsymbol{v})_{x=z} = 0, \tag{12}$$

for incompressible fluids and the equation of motion

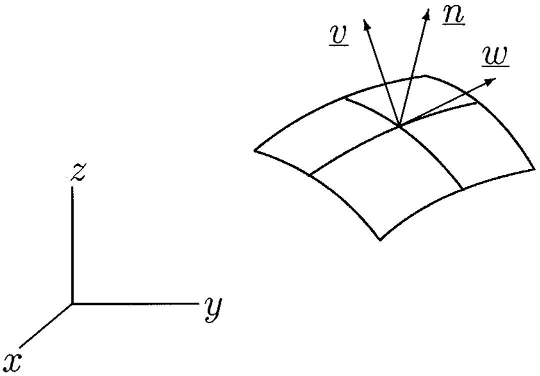

Figure 1. The free interface.

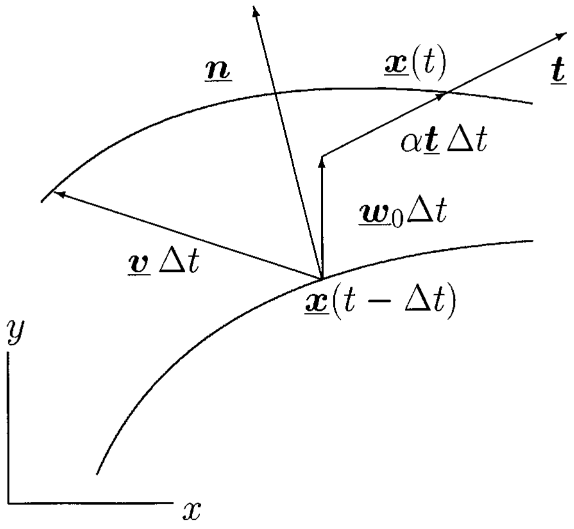

Figure 2. Definition of the spines, illustrated in 2D.

$$\rho\left(\frac{\partial\bar{\boldsymbol{v}}}{\partial t}+(\boldsymbol{v}-\boldsymbol{w})\cdot(\nabla\boldsymbol{v})_{x=z}\right)=-\nabla\cdot\boldsymbol{\pi}+\rho\boldsymbol{g}, \tag{13}$$

where $\bar{\boldsymbol{v}}(\xi,t)=\boldsymbol{v}(z_i(\xi,t),t)$ is the velocity of the observation point. $\boldsymbol{\pi}$ is the component of the total stress tensor. In the notation of Bird *et al.* [8]

$$\boldsymbol{\pi}=p\boldsymbol{\delta}-\boldsymbol{\tau}=p\boldsymbol{\delta}-\eta(\dot{\gamma})[(\nabla\boldsymbol{v})_{x=z}+(\nabla\boldsymbol{v})^{\dagger}_{x=z}], \tag{14}$$

for an incompressible generalized Newtonian fluid of viscosity η. $\boldsymbol{\delta}$ is the unit tensor, $\dot{\gamma}$ is the shear rate and † denotes the transpose operation. Equations (12) and (13) are both in agreement with Lamb [9].

3. FINITE ELEMENT FORMULATION

3.1. The free interface

The free interface positions are obtained by solving Equation (9). For reasons explained below, the streamline upwind/Petrov–Galerkin (SUPG) formulation [10] was used in order to discretize the equation. A slightly modified SUPG method is introduced to avoid oscillations due to differences in element size. The SUPG shape function is multiplied by $(\sqrt{J})^{-1}$ where J is the determinant of the metric tensor field on the discretized interface.

In the notation from Hughes *et al.* [11],

$$\int_{\Gamma_f}[(\hat{\boldsymbol{v}}-\hat{\boldsymbol{w}})\cdot\boldsymbol{n}]\tilde{\phi}^s\,\mathrm{d}\Gamma=0, \qquad \tilde{\phi}^s=\left[\phi^s+\frac{(\hat{\boldsymbol{v}}-\hat{\boldsymbol{w}})\cdot\nabla_s\phi^s}{|\boldsymbol{b}^e|_p}\right]\frac{1}{\sqrt{J}}, \tag{15}$$

with $s=1,\ldots,F$, where F is the total number of nodes on the interface. In this implementation the ϕ^i are trilinear shape functions. ∇_s is the gradient in the free interface or surface Γ_f, normally denoted as the surface divergence operator. The variables with a hat are approximate quantities. The $\boldsymbol{b}^e$ vector is defined as

$$\boldsymbol{b}^e = \begin{pmatrix} (\hat{\boldsymbol{v}} - \hat{\boldsymbol{w}}) \cdot \nabla_s \xi(\hat{\boldsymbol{x}}) \\ (\hat{\boldsymbol{v}} - \hat{\boldsymbol{w}}) \cdot \nabla_s \eta(\hat{\boldsymbol{x}}) \end{pmatrix}, \tag{16}$$

where (ξ, η) are the local element co-ordinates on the discretized interface and $\hat{\boldsymbol{x}}$ is the global interface position. Hence,

$$|\boldsymbol{b}^e|_p = (|(\hat{\boldsymbol{v}} - \hat{\boldsymbol{w}}) \cdot \nabla_s \xi|^p + |(\hat{\boldsymbol{v}} - \hat{\boldsymbol{w}}) \cdot \nabla_s \eta|^p)^{1/p}, \tag{17}$$

where $p = 2$ in this implementation. Moreover,

$$\sqrt{J} = \left| \frac{\partial \hat{\boldsymbol{x}}}{\partial \xi} \times \frac{\partial \hat{\boldsymbol{x}}}{\partial \eta} \right|, \tag{18}$$

defines the determinant of the interface or surface metric tensor field, and

$$\boldsymbol{n} = \left(\frac{\partial \hat{\boldsymbol{x}}}{\partial \xi} \times \frac{\partial \hat{\boldsymbol{x}}}{\partial \eta} \right) \frac{1}{\sqrt{J}}, \tag{19}$$

the outer normal vector to the surface, both at time t. Note that $\mathrm{d}\Gamma = \sqrt{J}\, \mathrm{d}\xi\, \mathrm{d}\eta$. When $\boldsymbol{n}$ from Equation (19) is inserted into (15) it is clear that (15) is a pure advection transport equation. This motivates the use of the SUPG method above.

The velocity of the fluid and the observation point is written as

$$\hat{v}_k = \sum_{i=1}^{N} v_k^i \phi^i, \tag{20}$$

and

$$\hat{w}_k = \sum_{i=1}^{N} w_k^i \phi^i, \tag{21}$$

respectively. N is the total number of nodes. Here the v_k^i is the kth component of the fluid velocity of node i, while w_k^i is the kth component of the velocity of the node itself. Thus, Equation (21) denotes a discretization of the mesh velocity. Similarly, the position of the observation point is discretized as

$$\hat{x}_k = \sum_{i=1}^{N} x_k^i \phi^i. \tag{22}$$

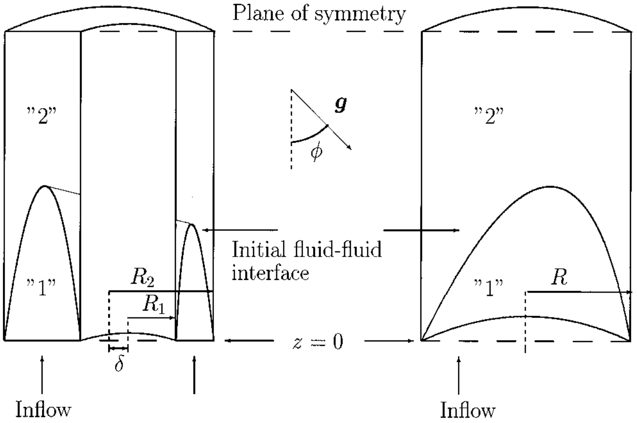

Figure 3. (a) The annular geometry; (b) The inclined tube.

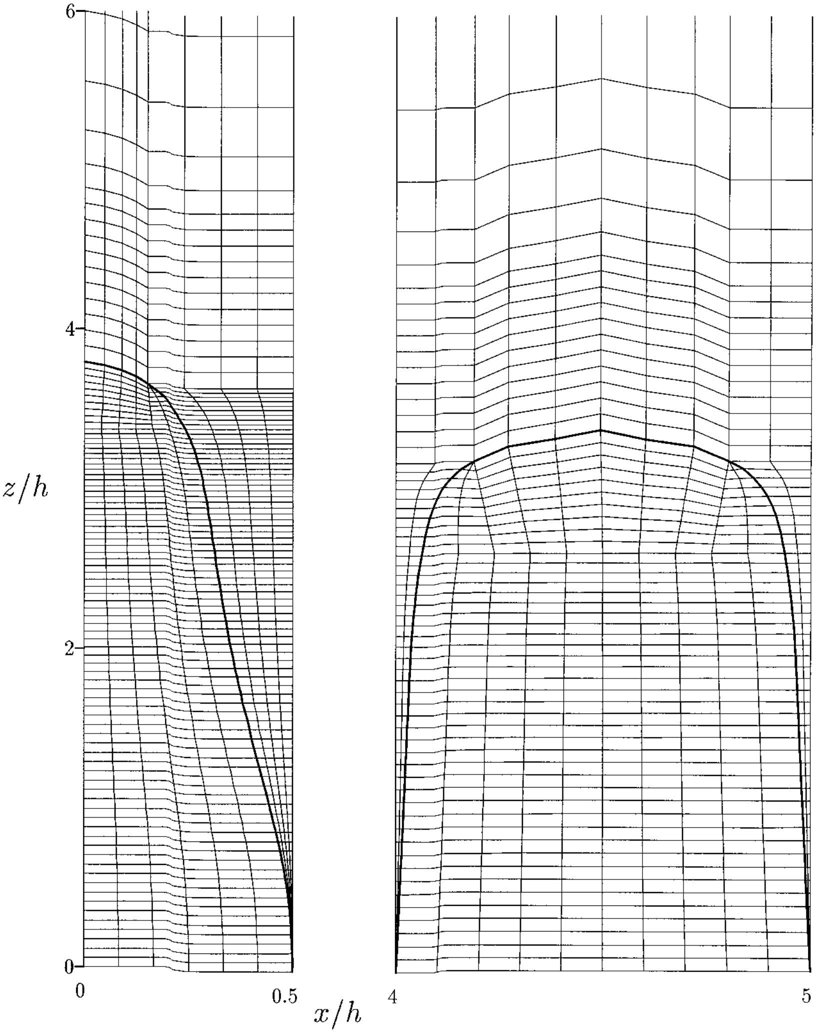

Figure 4. The meshes at the plane of symmetry used in the simulations. Left: the mesh in the tube. Right: the annular mesh. The thick lines are the free interfaces.

Although the velocities of the nodes on the interface must satisfy Equation (15), this condition is not sufficient to specify the w_k^i. Therefore, further relations are introduced:

$$w_k^i = w_{0,k}^i + \alpha^{s(i)} t_k^i. \tag{23}$$

Here, $w_{0,k}^i$ and t_k^i are fixed vectors that are specified to define the motion of the nodes. $w_{0,k}^i$ is the component of a preset velocity for all nodes, while t_k^i gives the direction of spines on which the interfacial nodes move (Figure 2).

The dependence between the positions and the velocities of the observation points is approximated through the implicit backward Euler scheme, as

$$w_{0,k}^i + \alpha^{s(i)} t_k^i = \frac{x_k^i(t) - x_k^i(t - \Delta t)}{\Delta t}, \tag{24}$$

where $\alpha^{s(i)}=0$ represents a node without a free interface. This relation provides a constraint that is used in the solution of the set of non-linear equations for the discrete variables in a manner described later.

At the free interface, the $\hat{\boldsymbol{w}}_0^i$ and $\hat{\boldsymbol{t}}^i$ parameters specify the movement of the observation point $\boldsymbol{x}^j$ to be restricted on predefined straight lines in space ('spines'), through Equation (24) as illustrated in Figure 2. This formulation allows a very large degree of freedom in the movement of a node.

3.2. The weak formulation

The discretization of Equations (13) and (12) follows the mixed Galerkin finite element method (see References [12,13]). The Galerkin weak form of Equation (13) is

$$\int_\Omega \rho\left[\frac{\partial\hat{\boldsymbol{v}}}{\partial t}+(\hat{\boldsymbol{v}}-\hat{\boldsymbol{w}})\cdot(\nabla\hat{\boldsymbol{v}})-\boldsymbol{g}\right]\phi^i\,\mathrm{d}\Omega-\int_\Omega \hat{\boldsymbol{\pi}}\cdot(\nabla\phi^i)\,\mathrm{d}\Omega+\int_{\Gamma_n}[\boldsymbol{n}\cdot\hat{\boldsymbol{\pi}}]\phi^i\,\mathrm{d}\Gamma=0, \tag{25}$$

with $i=1,\ldots,N$ and

$$\int_\Omega (\nabla\cdot\hat{\boldsymbol{v}})\psi^j\,\mathrm{d}\Omega=0, \tag{26}$$

where $j=1,\ldots,M$.

Ω denotes the fluid domain and Γ_n the surfaces with a natural boundary condition imposed.

The pressure field is approximated as

$$\hat{p}=\sum_{j=1}^{M}p^j\psi^j. \tag{27}$$

In the present implementation, shape functions ψ^j are used, and are constant in each element. The total number of pressure nodes is M.

The time derivative in Equation (25) is discretized through the implicit backward Euler scheme similar to Equation (24):

$$\frac{\partial\hat{\boldsymbol{v}}}{\partial t}=\frac{\hat{\boldsymbol{v}}(t)-\hat{\boldsymbol{v}}(t-\Delta t)}{\Delta t}. \tag{28}$$

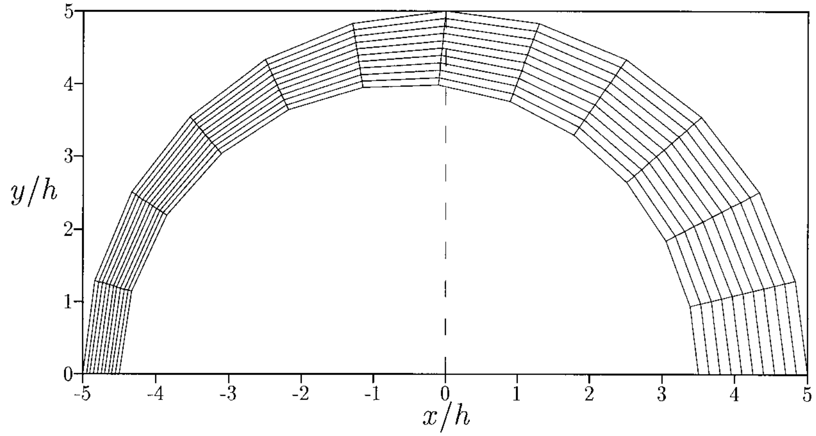

Figure 5. The inlet mesh ($z=0$) used in the simulations for the eccentric annulus.

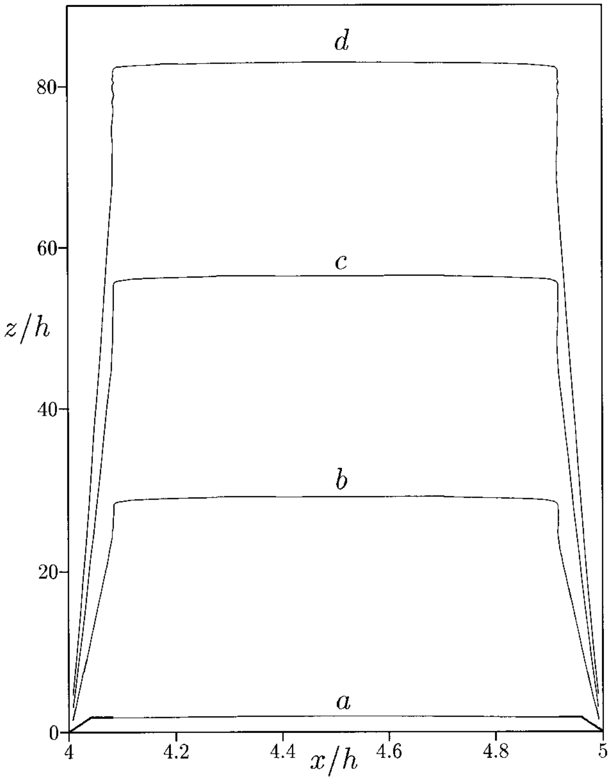

Figure 6. Development of the interface in a concentric annulus. The non-dimensional parameters are $Re_1 = Re_2 = 0$, $Ca^{-1} = 0$, $N_\mu = 1$, $Bu = 125$. The amount of fluid pumped is *a*: $\bar{z} = 1.8h$, *b*: $\bar{z} = 26.1h$, *c*: $\bar{z} = 50.5h$ and *d*: $\bar{z} = 74.2h$.

The Babuska–Brezzi stability condition [14] is not satisfied with constant pressure elements and trilinear shape functions. It is possible to obtain ‘checkerboard’ pressures or even non-converging pressure and velocity fields in this implementation. However, it appears that a proper choice of the finite element mesh avoids these problems.

3.3. The interface tension boundary condition

A 3D finite element representation of the interface tension boundary condition may be found in Ruschak’s work [15]. The notation of Szabo and Hassager [5] is used here:

$$\int_{\Gamma_{1,2}} [\boldsymbol{n} \cdot (\boldsymbol{\bar{\pi}}_1 - \boldsymbol{\bar{\pi}}_2)]\phi^i \, \mathrm{d}\Gamma = \int_{\gamma_c} \phi^i \sigma \boldsymbol{m} \, \mathrm{d}\gamma - \int_{\Gamma_{1,2}} \sigma(\boldsymbol{\nabla}_s \phi^i) \, \mathrm{d}\Gamma. \tag{29}$$

Here, σ is the surface tension coefficient and $\Gamma_{1,2}$ is the interface or surface with a surface tension boundary condition imposed. $\boldsymbol{m}$ is a unit vector, normal to and defined on the boundary γ_c of $\Gamma_{1,2}$. The contact angle is represented by $\boldsymbol{m}$.

3.4. The complete system of equations

We have arrived now at a total of $(9N + M + F)$ unknowns as follows:

$$v_k^i, w_k^i, x_k^i, \quad k = 1, 2, 3; \quad i = 1, \ldots, N, \tag{30}$$

$$p^j, \quad j = 1, \ldots, M, \tag{31}$$

$$\alpha^s, \quad s = 1, \ldots, F. \tag{32}$$

The corresponding equations are given by Equations (25), (23), (24), (26) and (15), where the total number of equations are $3N$, $3N$, $3N$, M and F, respectively. In compact notation

$$\boldsymbol{R}(\hat{\boldsymbol{p}}, \hat{\boldsymbol{v}}, \hat{\boldsymbol{w}}, \hat{\boldsymbol{x}}, \boldsymbol{\alpha}) = 0. \tag{33}$$

Taking advantage of the simplicity of Equations (23) and (24), we have eliminated the unknowns w^i_k and x^i_k in the system of equations. Hence, the resulting method involves the computation of all the velocities, pressures and α coefficients in each time step from

$$\boldsymbol{R}^*(\hat{\boldsymbol{p}}, \hat{\boldsymbol{v}}, \boldsymbol{\alpha}) = \boldsymbol{R}(\hat{\boldsymbol{p}}, \hat{\boldsymbol{v}}, \hat{\boldsymbol{w}}(\boldsymbol{\alpha}), \hat{\boldsymbol{x}}(\boldsymbol{\alpha})) = 0. \tag{34}$$

The Newton iteration is used to solve the equations. The derivatives with respect to the element pressures and node velocities in the Newton iteration are straightforward, whereas the derivatives with respect to the α coefficients are more complex:

$$\frac{\partial R^*_r}{\partial \alpha^s} = \sum_j \sum_k \frac{\partial R_r}{\partial x^j_k} \frac{\partial x^j_k}{\partial \alpha^s} + \sum_j \sum_k \frac{\partial R_r}{\partial w^j_k} \frac{\partial w^j_k}{\partial \alpha^s} = \Delta t \sum_{k=1}^{3} t^{i(s)}_k \cdot \frac{\partial R_r}{\partial x^{i(s)}_k} + \sum_{k=1}^{3} t^{i(s)}_k \cdot \frac{\partial R_r}{\partial w^{i(s)}_k}, \tag{35}$$

because of the dependence between the positions and velocities of the observation points and the α coefficients through Equations (24) and (23), since t^i_k is constant during one time step.

4. THE MESH DISPLACEMENT STRATEGY

Several alternative displacement strategies have been proposed in the literature, including the grid re-zoning method from Szabo [17], the semi-Lagrange method [2] or the more arbitrary method of Doneai *et al.* [18]. Generally, the problem with these methods is that, although they may be useful in interior flow domains, they are less applicable at the free interface. Other methods are useful at the free interface, but do not allow large free interfacial and interior node motions.

In the present technique, the vectors $\boldsymbol{w}^i_0$ and $\boldsymbol{t}^i$ are as yet unspecified parameters to be used for the mesh displacement. Note that it is possible in principle for all $\boldsymbol{w}^i_0 = \boldsymbol{0}$ (but $\boldsymbol{t}^i \neq \boldsymbol{0}$). Then all interior nodes are fixed and it is just the interface nodes that move. Clearly this may produce overly distorted elements close to the interface after even a few time steps. Consequently, it is advantageous to remesh the interior domain also in each time step. The method in which the $\boldsymbol{w}^i_0$ are determined for this purpose is now described. The procedure is divided into three parts.

1. The first part is a preliminary prediction of the positions of the new interface at time t, where subscript p denotes the predicted value. The positions are given by the mesh velocities $w^i_{0,k}(t - \Delta t)$, or in terms of the co-ordinates

   $$[x^{i(s)}_k]_p = w^{i(s)}_{0,k}(t - \Delta t) \cdot \Delta t + x^{i(s)}_k(t - \Delta t), \quad s = 1, \ldots, F. \tag{36}$$

   Equation (36) represents a linear extrapolation.
2. The second part is a remesh, denoted subscript r, of the interface from the predicted interface positions $[x^{i(s)}_k]_p$. This method allows the interface nodes to be positioned in the area of the interface where they are needed.

3. Finally, it becomes necessary to determine new nodes in the interior flow domain, denoted subscript r, including the boundary that is not part of the interface.

The specified mesh velocities $\boldsymbol{w}_0$ (Equation (24)) are then obtained from

$$w^i_{0,k} = \frac{[x^i_k]_r + x^i_k(t - \Delta t)}{\Delta t}, \quad i = 1, \ldots, N. \tag{37}$$

It remains to specify the vectors $\boldsymbol{t}^i$. These vectors, together with the $\boldsymbol{w}^i_0$, define the linear spines on which the interface nodes move. Therefore, the $\boldsymbol{t}^i$ are adjusted to obtain a desired location of the interface spines. In each specific flow problem, however, the spines must be positioned from a physical expectation of evolution of the interface. A good choice of the $\boldsymbol{t}^i$ is often close to the normal of the interface.

5. NON-DIMENSIONAL GROUPS IN DISPLACEMENT

The applicability of the technique is illustrated by simulations of fluid–fluid displacement in two specific geometries, namely a vertical eccentric annulus and a inclined tube, as shown in Figure 3(a,b), respectively.

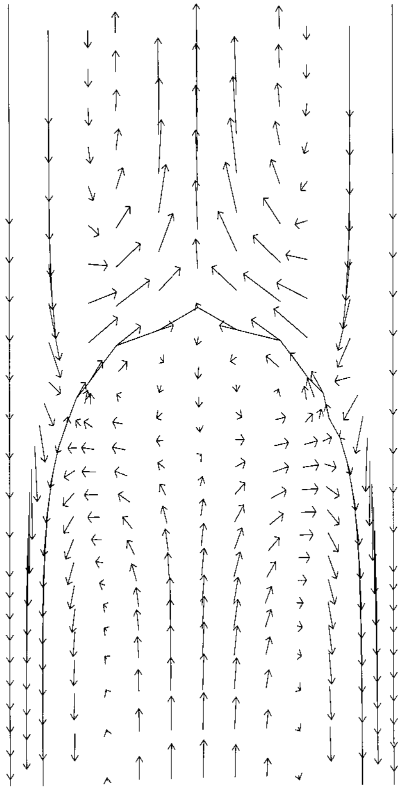

Figure 7. The steady velocity field in a reference system following the interface front. The simulation is the same as in Figure 6 ($\bar{z} = 50.5h$).

Non-dimensionalization of the equations of continuity and motion is considered below. The non-dimensionalization is similar to Szabo and Hassager [6].

The geometrical variables in the annulus are: the inner radius R_1, the outer radius R_2 and the displacement of the inner tube from the center of the outer tube, δ. This allows the definition of two geometrical dimensionless groups as the ratio between the radii, $\kappa = R_1/R_2$, and the eccentricity, $e = \delta/(R_2 - R_1)$. The only geometrical variable in the tube is the radius, R. Moreover, h is defined as a characteristic length scale in the annulus and tube, given as $h = R_2 - R_1$ and $h = 2 \cdot R$, respectively.

The two fluid phases in the displacement are characterized by the fluid densities, ρ_1 and ρ_2, and viscosities, μ_1 and μ_2. Index 1 represents the displacing fluid and index 2 the displaced fluid. $\boldsymbol{g}$ is the gravitational acceleration and ϕ is the angle of inclination of the tube axis.

We specify a fully developed uni-directional laminar velocity profile, characterized by an average velocity $\bar{v}$, at the inlet ($z = 0$). The average velocity, $\bar{v}$, is defined as the volume rate of flow divided by the cross-sectional area of the geometry.

In order to introduce non-dimensional groups in the displacement problem, the variables are non-dimensionalized as $\boldsymbol{v}^* = \boldsymbol{v}/\bar{v}$, $\boldsymbol{w}^* = \boldsymbol{w}/\bar{v}$, $t^* = t\bar{v}/h$, $\boldsymbol{\chi} = \boldsymbol{g}/g$, and $\mathscr{P}^* = \mathscr{P}h/(\mu_1\bar{v})$. $\mathscr{P}$ is the modified pressure, defined from $-\nabla\mathscr{P} = -\nabla \mathrm{p} + \rho_2\boldsymbol{g}$. Hence, the non-dimensional equation of motion is

$$Re_1\left(\frac{\mathrm{d}\boldsymbol{v}^*}{\mathrm{d}t^*} + (\boldsymbol{v}^* - \boldsymbol{w}^*)\cdot\boldsymbol{\nabla}^*\boldsymbol{v}^*\right) = -\boldsymbol{\nabla}^*\mathscr{P}^* + \nabla^{*2}\boldsymbol{v}^* + Bu\boldsymbol{\chi}, \tag{38}$$

in the displacing fluid, fluid phase 1, and

$$N_\mu Re_2\left(\frac{\mathrm{d}\boldsymbol{v}^*}{\mathrm{d}t^*} + (\boldsymbol{v}^* - \boldsymbol{w}^*)\cdot\boldsymbol{\nabla}^*\boldsymbol{v}^*\right) = -\boldsymbol{\nabla}^*\mathscr{P}^* + N_\mu\nabla^{*2}\boldsymbol{v}^*, \tag{39}$$

in the displaced fluid, fluid phase 2.

Finally, the non-dimensionalized equation of mass conservation—in both fluid phases—is stated in the form

$$\boldsymbol{\nabla}^*\cdot\boldsymbol{v}^* = 0. \tag{40}$$

The above equations depend upon four dimensionless groups and the non-dimensional vector $\boldsymbol{\chi}$. The groups can be interpreted as the Reynolds number in fluid phase m

$$Re_m = \frac{h\bar{v}\rho_m}{\mu_m}, \quad m = 1, 2, \tag{41}$$

the buoyancy number [1]

$$Bu = \frac{(\rho_1 - \rho_2)gh^2}{\bar{v}\mu_1}, \tag{42}$$

and the viscosity ratio

$$N_\mu = \frac{\mu_2}{\mu_1}. \tag{43}$$

Finally, the non-dimensional interface or surface tension, the capillary number, is defined as

$$Ca = \frac{\mu_1\bar{v}}{\sigma}, \tag{44}$$

which is the ratio between the viscous forces and surface tension forces.

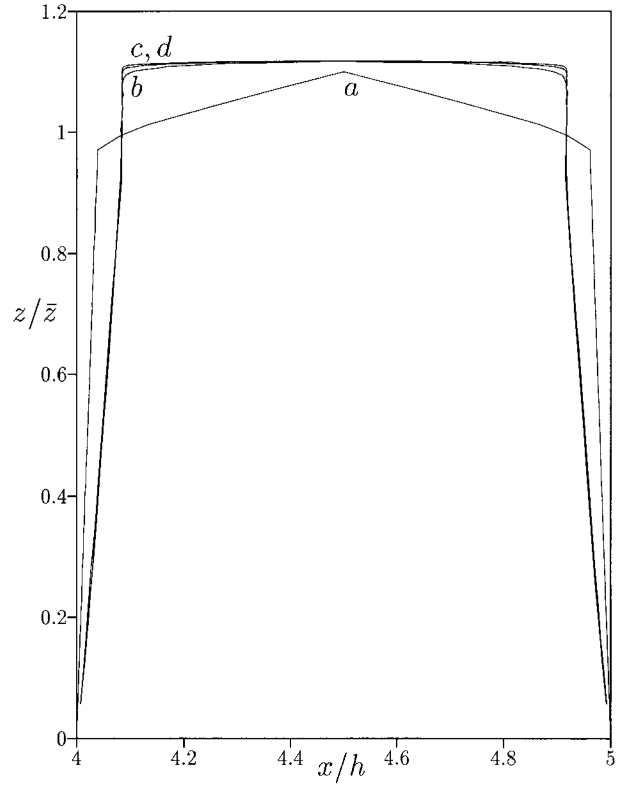

Figure 8. Development of the interface in a concentric annulus. The interfaces are scaled in the longitudinal direction by the total amount of fluid pumped, $\bar{z}$. The simulation is the same as Figure 6.

No further parameters are introduced by χ for the vertical annulus, whereas for the inclined tube, χ introduces the angle ϕ.

The results of simulations of the displacement of one Newtonian fluid by another are presented below.

6. TIME AND SPATIAL DISCRETIZATION

The geometries of the simulations are shown in Figure 3. In order to have a well-defined mathematical problem, the boundary conditions are specified as the no-slip condition on the walls of the geometry, fully developed Poiseuille velocity field at the inlet ($z = 0$), no flow perpendicular to the symmetry plane, the initial condition at $t^* = 0$ and a constant pressure at the outlet. The outlet is at a position $10h$ above the top of the displacing fluid. Thus, the outlet is continually moved during simulations. The initial velocities are zero and the initial position of the interface is specified in each simulation.

The meshes used in the simulations are illustrated in Figure 4, right and left for the annular and the tube geometry, respectively. The thick line is the free interface. The mesh is gradually expanded as the interface evolves in time (see Section 4). The tube and the concentric annulus are divided into eight identical elements in the azimuthal direction in the xy-plane. Moreover, the eccentric annulus is divided into 12 elements in the azimuthal direction as illustrated in Figure 5 for $z = 0$. The increased number of elements is needed in order to resolve the flow in the azimuthal direction.

The method may be used with variable time steps. The initial Δt^* is 0.02, and is gradually increased by a factor of 1.104 in each time step. Towards the end of the simulations a step length of $\approx 10\%$ of the total time was applied.

7. ANNULAR DISPLACEMENT

Annular displacement simulations were performed at buoyancy numbers between 125 and 500, viscosity ratio $N_\mu = 1$, the ratio between the radii $\kappa = 0.8$, and the eccentricity $e = 0.5$ and 0. This corresponds to an experimental study by Long [16]. In the present study, the flow in creeping motion ($Re_1 = Re_2 = 0$) is considered.

7.1. Concentric annular displacement

The transient development of the interface in the concentric annulus at $Bu = 125$ is shown in Figure 6 for several amounts of fluid pumped. As a measure of the total amount of fluid pumped, $\bar{z}$ is defined as $\bar{z} = \bar{v} \cdot t$.

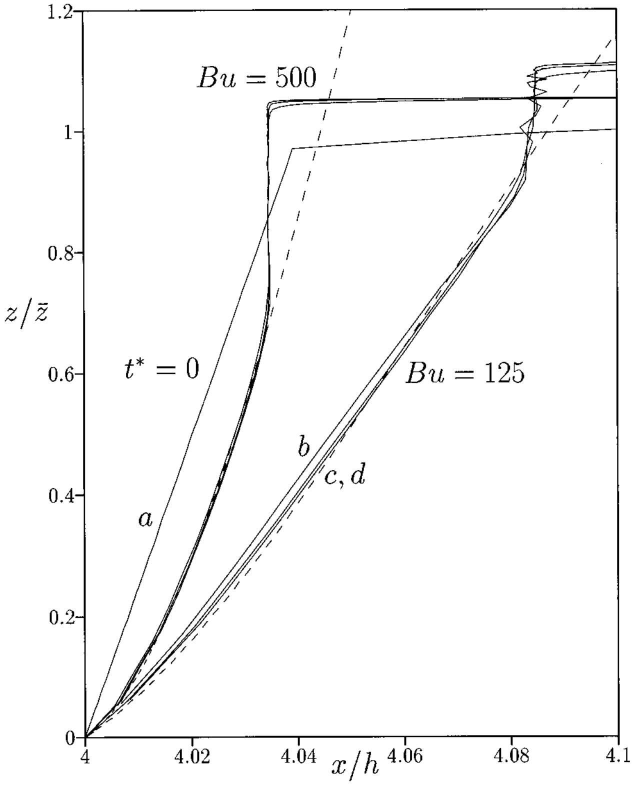

Figure 9. Enlargement of Figure 8 near the inner cylinder. The solid lines are simulations at $Bu = 125$ and 500. The amount of fluid pumped is $\bar{z} = 1.8h$ (a), $\bar{z} = 26.0h$, $\bar{z} = 50.3h$ and $\bar{z} = 74.0h$ for $Bu = 500$. The simulation for $Bu = 125$ is the same as Figure 6. The dashed lines are the lubrication theory.

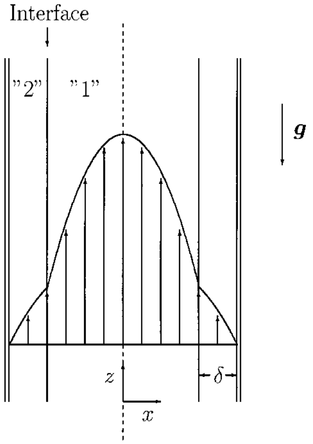

Figure 10. Flow of two immiscible fluids between two flat planes under the influence of a pressure gradient and gravity. The dashed line is the plane of symmetry.

In order to gain information about the process that induces the flat interface, the velocity field is drawn in Figure 7 at a buoyancy number of 125. The velocity is obtained by subtracting the velocity of the front from the actual velocity field. This corresponds to a reference system following the interface front. It appears that the different fluid densities force recirculations to occur both behind and above the interface in opposite directions. Hence, the recirculations force vortices to be situated below the interface. Moreover, as an effect of these vortices, the interface in a reference system following the interface front develops a piston-like steady flow. The same flow behaviour was observed experimentally by Long [16].

In Figure 8 the interface curves from Figure 6 are scaled—in the longitudinal direction—by the total amount of fluid pumped, $\bar{z}$. It seems that all the interface curves coincide when a large amount of fluid has been pumped. These curves (the solid lines) are scaled up near the inner cylinder (Figure 9), in order to show the film layer near the wall. A computation at $Bu = 500$ is included in Figure 9. If wiggles appear in the interface, as is the case at $Bu = 125$ and $\bar{z}/h = 74.1$, the time integration breaks down in a few time steps. The explanation is that the discretization in the longitudinal direction is too coarse to resolve the velocity field properly near the fluid front. It appears that by increasing the number of elements in the longitudinal direction, much further integration in time is possible. The development of the wiggles is insensitive to the time step-length.

The dashed lines in Figure 9 represent a simple lubrication theory [19,20]. An important effect found from the lubrication theory is that the interface curves scaled by the total amount of fluid coincide as large quantities of fluid are pumped. In the lubrication theory the flow in the annular gap is approximated as (vertical) slit flow (Figure 10). The gap width in the annulus is used as the distance between the two plates in the slit. The predictions of the lubrication theory provide good agreement with the simulations, especially at $Bu = 500$ where the geometrical effects are unimportant. On the contrary, the lubrication theory cannot predict the frontal shape of the displacing fluid and the theory is only valid in the vertical situations.

We note in closing that the scaling of the interface curves predicted by the lubrication theory and confirmed by the simulations has a far reaching consequence. In numerical and experimental displacement studies, moderate aspect ratios of length to diameter are by necessity used. By contrast, in practical drilling situations, the relevant aspect ratio will typically be one to three orders of magnitude larger. When the domains scale with the amount of fluid pumped, however, it is in fact possible to obtain useful information from simulations or experiments in the range of aspect ratios shown here.

7.2. Eccentric annular displacement

The transient development of the interface in the eccentric ($e = 0.5$) annulus at $Bu = 125$ is shown in Figure 11 for several amounts of fluid pumped. A small amount of interface tension ($Ca = 0.5$) is imposed in order to stabilize the interface. The effect of the interface tension on the interface position below the fluid front is negligible, but a small effect on the frontal shape of the interface is observed. The simulations show a relatively small variation in the position of the fluid front with the azimuthal angle and a relatively larger amount of displaced fluid in the narrow gap compared with the wide part of the annulus. The same qualitative behaviour of the interface positions were observed by Long [16].

In order to gain information about the process that induces the flat interface profile, the steady velocity field in a reference system following the interface front is shown in Figure 12. In the wide part of the annulus the flow is similar to the concentric simulation. Due to the wider gap, however, the vortices behind the interface are suppressed by a higher local buoyancy number.

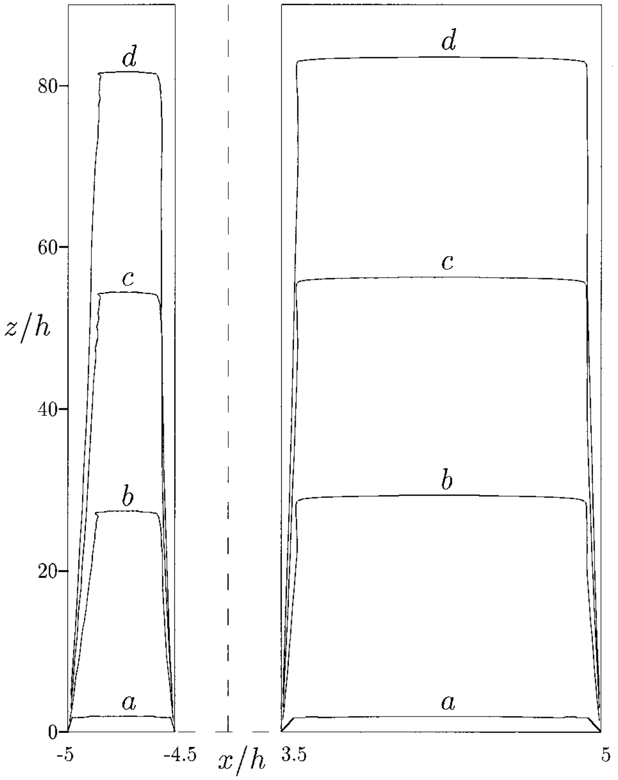

Figure 11. Development of the interface in an eccentric, $e = 0.5$, annulus at the plane of symmetry. Note, the narrow and the wide part of the annulus have been shifted towards the center of the annulus in the figure. The non-dimensional parameters are $Re_1 = Re_2 = 0$, $Ca = 0.5$, $N_\mu = 1$, $Bu = 125$. The amount of fluid pumped is *a*: $\bar{z} = 1.8h$, *b*: $\bar{z} = 26.0h$, *c*: $\bar{z} = 50.3h$ and *d*: $\bar{z} = 75.0h$.

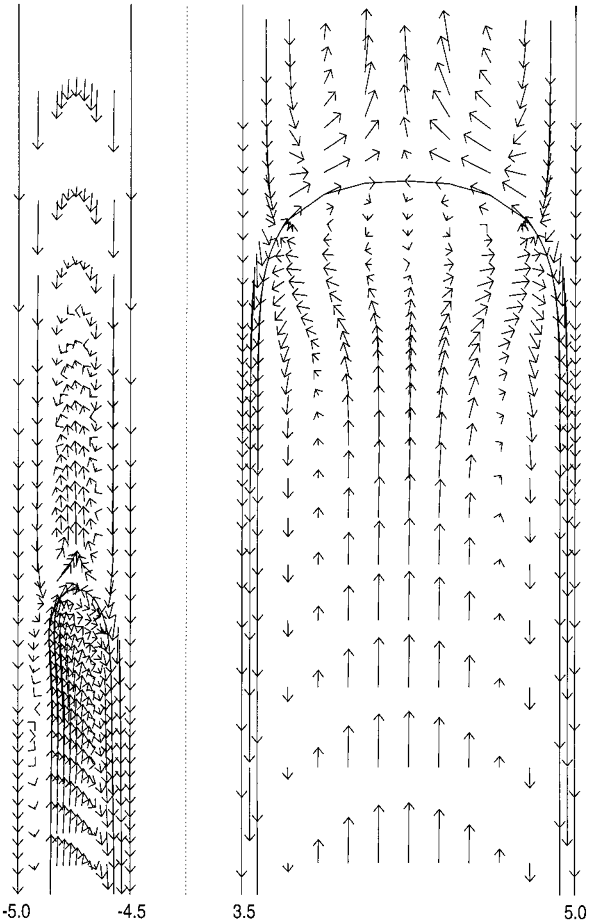

Figure 12. The steady velocity field in a reference system following the interface front at the plane of symmetry. Note, the narrow and the wide part of the annulus have been shifted towards the center of the annulus in the figure. This is similar to Figure 11. The simulation corresponds to the one in Figure 11 ($\bar{z} = 50.3h$).

The fluid in the displacing phase originates from the inlet. On the contrary, the maximum velocity of the inlet in the narrow part of the annulus is lower than the velocity of the front. Consequently, a larger part, if not all of the displacing fluid in the narrow part of the annulus, originates from redistribution of the fluid in the azimuthal direction. This redistribution flow appears to produce an asymmetrical velocity profile in the displacing fluid in the narrow part of the annulus.

In Figure 13 the interface curves from Figure 11 are scaled—in the longitudinal direction—by the total amount of fluid pumped, $\bar{z}$. As shown here, the interface curves (in the plane of symmetry) coincide at a large amount of fluid pumped. Hence, scaling of least in the plane of symmetry is again observed.

In order to investigate whether a scaling of the interface positions would make them coincide away from the symmetry plane also, a new variable, Φ, is introduced. Φ is the fraction of the displaced fluid (fluid 2) in the annulus in a plane perpendicular to the z-axis. In Figure 14, Φ is shown as a function of $z/\bar{z}$ for $Bu = 125$ and 250. Here, the fraction of displaced fluid coincides at a large amount of fluid pumped. This indicates that a lubrication theory extended to eccentric annulus can describe the displacement.

Normally the quality of a fluid–fluid displacement is measured according to Tehrani *et al.* [1]. The displacement efficiency, E, is defined as the volume fraction of the displacing fluid (fluid 1) in an annulus of length L, as

$$E(t)=\int_{o}^{L}[1-\Phi(z,t)]A\,\mathrm{d}z/V \quad \text{or} \quad 1-E(t)=\int_{o}^{L}\Phi(z,t)A\,\mathrm{d}z/V, \tag{45}$$

where V is the volume and A the cross-sectional area of the annular section. The fraction of the displacing fluid as function of the time t and position z is $1-\Phi(z,t)$. Equation (45) can be written as

$$1-E(t)=\bar{z}/L\int_{o}^{L/\bar{z}}\Phi(z/\bar{z},t)\,\mathrm{d}(z/\bar{z}). \tag{46}$$

Moreover, if a non-dimensional time is defined as $T^{*}=t\bar{v}/L=\bar{z}/L$, it is the definition of the efficiency

$$1-E(T^{*})=T^{*}\int_{o}^{1/T^{*}}\Phi(z/\bar{z},t)\,\mathrm{d}(z/\bar{z}). \tag{47}$$

T^{*} corresponds to the amount of annular volume pumped.

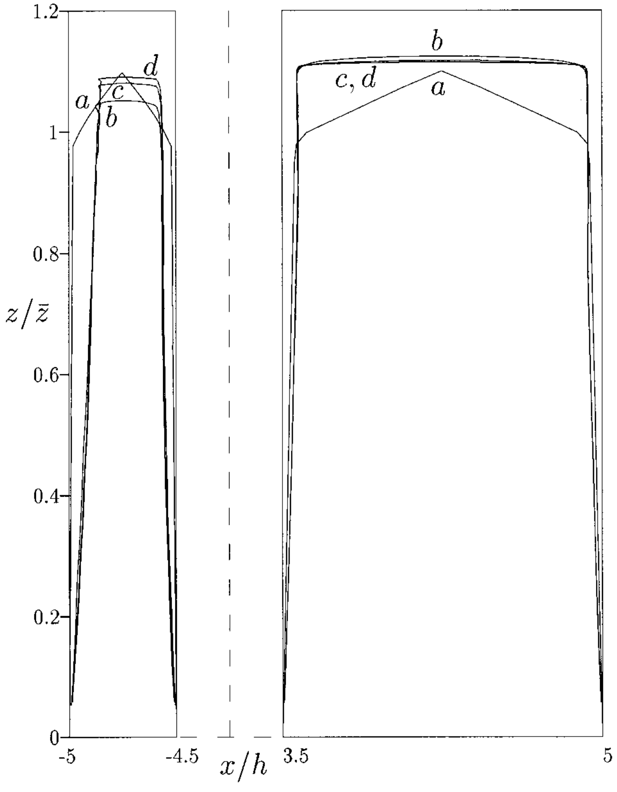

Figure 13. Development in the interface in the annulus at the plane of symmetry. The interfaces are scaled in the longitudinal direction by the total amount of fluid pumped, $\bar{z}$. The simulation is the same as Figure 11.

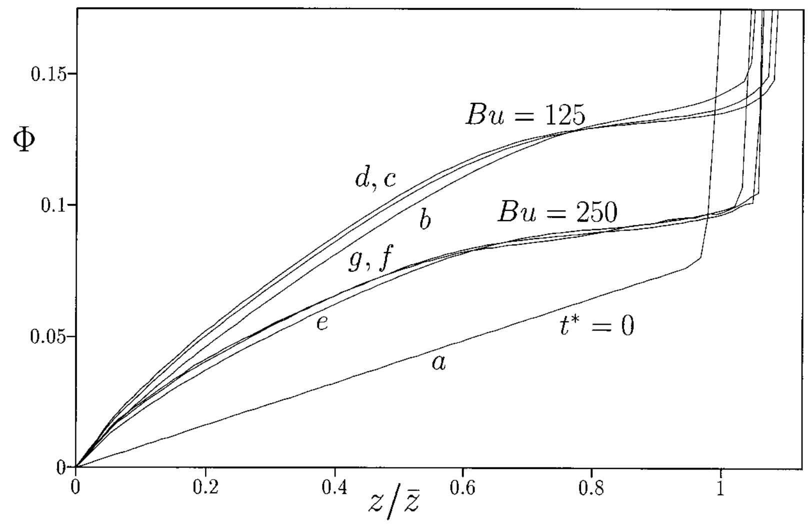

Figure 14. The fraction of the displaced fluid in a plane normal to the z-axis (Φ) as a function of $z/\bar{z}$. The amount of fluid pumped is a: $\bar{z}=1.8h$, e: $\bar{z}=20.0h$, f: $\bar{z}=41.8h$ and g: $\bar{z}=59.7h$ for $Bu=250$. The simulation for $Bu=125$ is the same as Figure 11.

The Φ curves in Figure 14 coincide at high t. Hence, $\Phi(z/\bar{z}, t)$ is independent of t. As Φ is independent of t, the co-ordinates may be suppressed in $\Phi(z/\bar{z}, t)$ to write $\Phi(z/\bar{z})$. The efficiency in Equation (47) is then written as

$$1-E(T^*)=T^*\int_{o}^{1/T^*}\Phi(z/\bar{z})\,\mathrm{d}(z/\bar{z}). \tag{48}$$

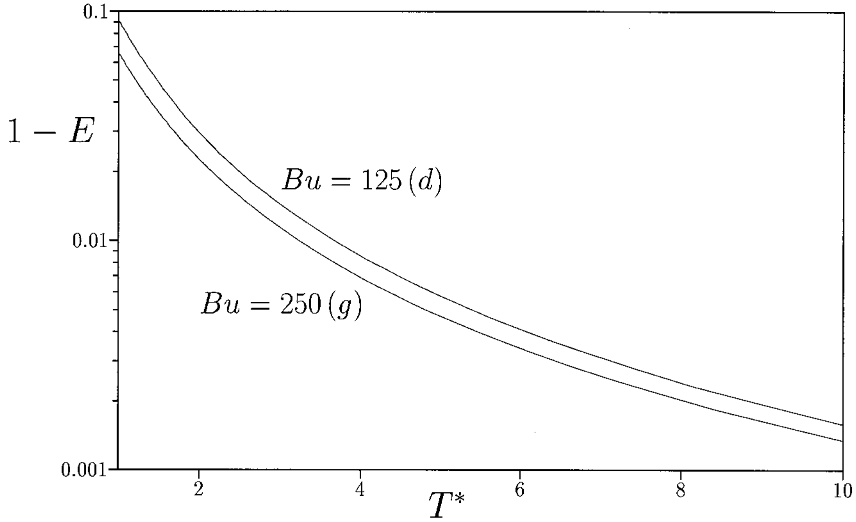

Figure 15. The displacement efficiency (e.g. $1-E$) as a function of the non-dimensional amount of annular volume pumped T^*. The simulation is the same as in Figure 14 (the curves d and g).

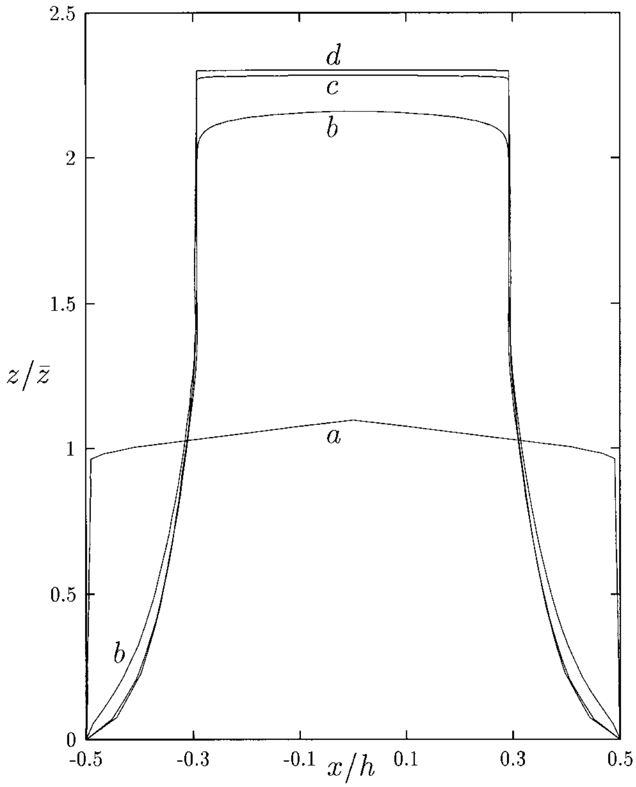

Figure 16. Development in the interface in a vertical tube. The interfaces are scaled in the longitudinal direction by the total amount of fluid pumped, $\bar{z}$. The non-dimensional parameters are $Re_1 = Re_2 = Ca^{-1} = Bu = 0$ and $N_\mu = 10$. The amount of fluid pumped is *a*: $\bar{z} = 0.9h$, *b*: $\bar{z} = 11.0h$, *c*: $\bar{z} = 109h$ and *d*: $\bar{z} = 1052h$.

Figure 15 shows the efficiency as a function of T^* after the breakthrough. The efficiencies are calculated from Equation (48) and the Φ curves in Figure 14.

8. DISPLACEMENT IN THE TUBE

As a further illustration of the method, the fluid–fluid displacement in a tube is considered. Displacement simulations were performed in order to investigate the effects of viscosity differences, inertia, interface tension and pipe inclination.

A vertical tube is under consideration in Figures 16–18. In Figure 16 the scaled interfaces for a viscosity ratio $N_\mu = 10$ ($Bu = Ca^{-1} = Re_1 = Re_2 = 0$) are shown. Note that $\bar{z} > 11h$ is needed to obtain an accurate determination of the final shape of the interface. At curve (*d*) $\bar{z}$ was larger than $1000h$.

The steady velocity field in a reference system following the interface front is shown in Figure 17. It appears that the difference in fluid viscosity forces recirculations to occur behind the interface. Above the interface, the fluid is moved from the center to the wall region. Due to the low viscosity in the displacing fluid, this behaviour corresponds to a gas displacing a fluid [21].

The effects of viscosity differences, interface tension and inertia are investigated in Figure 18. The curves are all the scaling interface curves at steady state. Interface *b* corresponds to Figure 16 and the Reynolds numbers are increased from 0 to $Re_1 = N_\mu Re_2 = 250$ at interface *a*. Hence, a small effect on the frontal shape of the interface is observed. In contrast to this, there is no effect of inertia on the lower region. This is in accordance with the lubrication theory.

Curve *d* is the (analytical) Poiseuille velocity field. In the simulation, curve *e*, the two fluid phases are the same, but a small amount of interface tension is imposed ($Ca = 1$). The same effect on the frontal shape and the lower region is observed as in curves *a* and *b*. The lower region of curves *e* and *d* coincide, but the interface tension seems to develop a piston-like frontal flow. The Poiseuille flow develops a vertex which is smoothed by the interface tension.

Interface curve *c* is calculated at viscosity ratio $N_\mu = 3$ ($Bu = Ca^{-i} = Re_1 = Re_2 = 0$) in order to illustrate the shift between Poiseuille flow and $N_\mu = 10$.

In Figure 19 the effect of pipe inclination is investigated. The interface curves correspond to Figure 16, but a small buoyancy, $Bu = 2$, is imposed. The inclination of the tube from vertical is $\phi = \pi/6$ (horizontal is equal to $\pi/2$). Hence, the effective buoyancy number parallel to the gravitational acceleration is $Bu \sin(\pi/6) = 1$. The effects are pronounced. There is a very small effect on the frontal shape, but behind the front the moving displacing fluid is shifted towards the tube wall. In this situation the scaling behavior observed for the vertical pipes and annuli does not appear to develop.

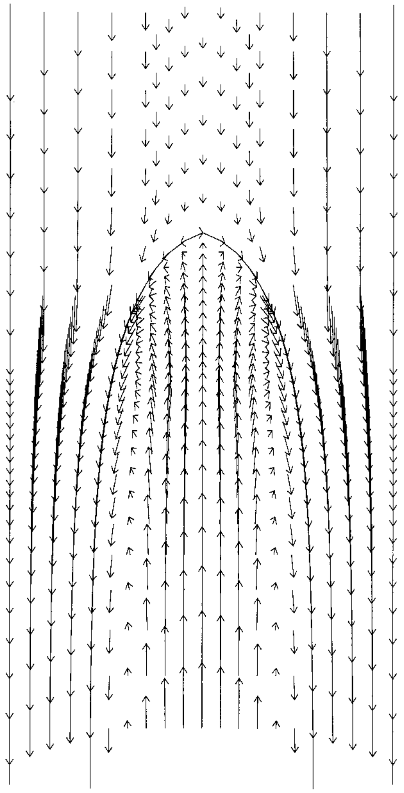

Figure 17. The steady velocity field in a reference system following the interface front. The simulation corresponds to Figure 16 ($\bar{z} = 196h$).

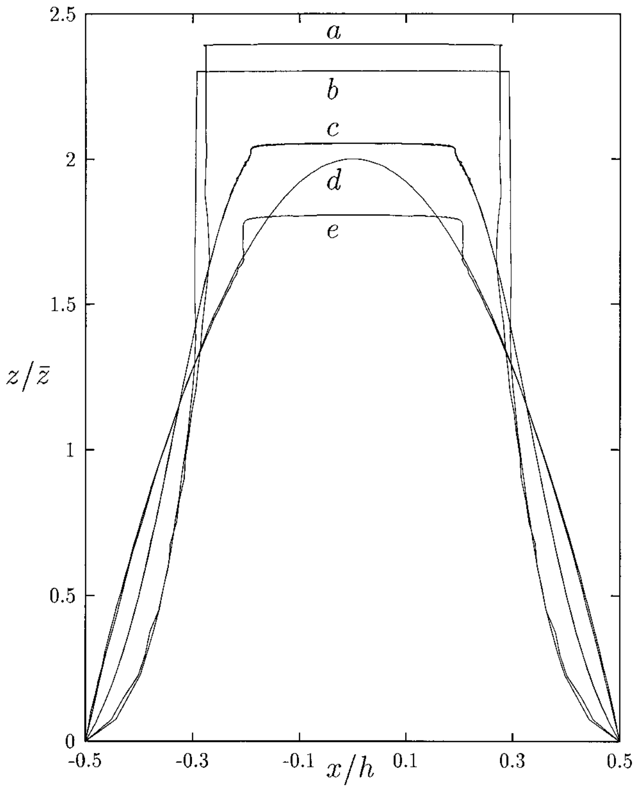

Figure 18. The development of the interface in a vertical tube. The curves are interfaces scaled by $\bar{z}$. The buoyancy number $Bu = 0$. The parameters $(N_\mu, Ca^{-1}, Re_1, Re_2, \bar{z}/h)$ are *a*: (10, 0, 250, 25, 190), *b*: (10, 0, 0, 0, 1052), *c*: (3, 0, 0, 0, 133) and *e*: (1, 1, 0, 0, 41). Interface *d* is a fully developed Poiseuille flow.

9. CONCLUSION

An arbitrary Lagrange–Euler finite element method was developed for 3D flow of generalized Newtonian fluids. The application of a streamline upwind Petrov–Galerkin formulation of the interface condition enables the method to handle a very large displacement of interfaces.

The method can handle a large displacement in each time step: a step length of $\approx 10\%$ of the total time was applied in the simulations. An extension of this method to a flow with sharp edges can be found in the Appendix.

This method represents a major improvement to the previous developments. The total amount of fluid pumped, $\bar{z}$, by Szabo and Hassager [6]was less than $9h$ in all simulations. Considerably higher amounts of fluid pumped are needed in order to draw definitive conclusions about displacement problems, especially in the eccentric and inclined situations.

Computations have been performed in a tube and an annulus. In the vertical situations, the interface curves coincide if the interface is scaled with the total amount of fluid pumped. The scaled interfaces can be predicted by a lubrication theory. However, the lubrication theory cannot predict the frontal shape of the displacing fluid and the theory is only valid in the vertical situations. The frontal flow develops a steady velocity field in these simulations.

A small effect of inertia on the frontal shape of the interface is observed, but there is no effect of inertia on the lower region, because the velocities transversing to the main flow are negligible.

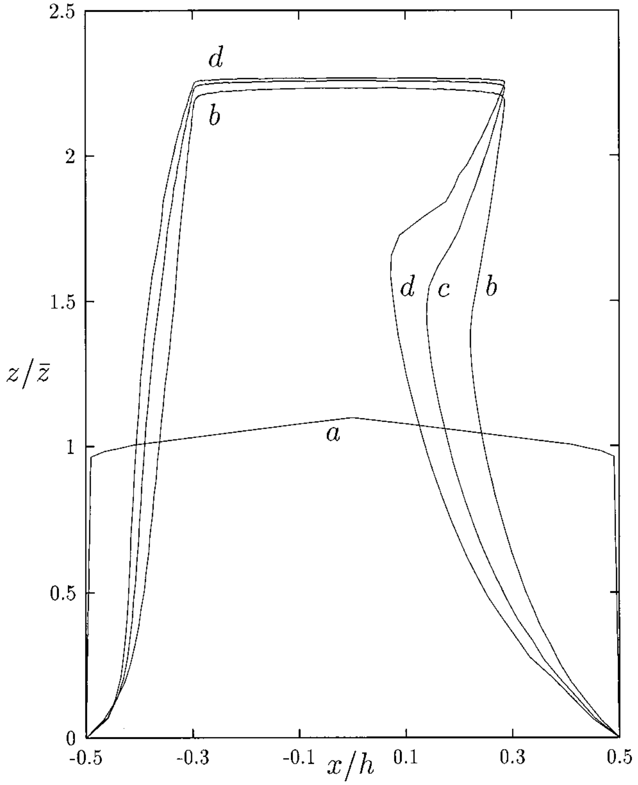

Figure 19. The development of the interface in the inclined ($\phi = \pi/6$) tube at the plane of symmetry. The curves are interfaces scaled by $\bar{z}$. The simulation corresponds to Figure 16 with a buoyancy number $Bu = 2$. The amount of fluid pumped is a: $\bar{z} = 0.9h$, b: $\bar{z} = 33.9h$, c: $\bar{z} = 66.8h$ and d: $\bar{z} = 98.7h$.

The mechanism in the inclined situation is not fully understood. The behavior of the interface when a large amount of fluid is pumped is an open question that requires further investigation.

ACKNOWLEDGMENTS

We would like to thank Shell Research B.V., Rijswijk and the Danish Polymer Centre (DPC) for the financial support. Finally we would like to thank Professor van den Brule, Drs. Ten Bosch and Szabo for many helpful discussions.

APPENDIX A. FLOW WITH SHARP EDGES

The method described in Section 3.1 refers only to a situation with smooth interfaces or surfaces as discussed by Wambersie and Crochet [22]. In 3D profile extrusion flows sharp edges on the free surface may occur. Another situation occurs whenever three phases meet, such as in two phase injection moulding. In order to handle sharp edges, an extension of the principle in Section 3.1 from arbitrary surfaces to arbitrary lines is needed.

A 1D line (an edge) in a 3D flow domain is defined as the intersection of the two surfaces $h_1(t, \boldsymbol{x}) = 0$ and $h_2(t, \boldsymbol{x}) = 0$. The kinematic description of a free line on the interface requires that the line is a material line. Hence, the material line equations are stated as

$$(\boldsymbol{v} - \boldsymbol{w}) \cdot \boldsymbol{n} = 0, \quad z \in \Gamma_1 \quad \text{and} \quad (\boldsymbol{v} - \boldsymbol{w}) \cdot \boldsymbol{n} = 0, \quad z \in \Gamma_2, \tag{49}$$

where Γ_1 and Γ_2 are the two different surfaces or interfaces. These two equations are solved similarly to Equation (15) for each node on the material line.

The movement of the observation point is then approximated through

$$\hat{w}_k^i = \hat{w}_{0,k}^i + \hat{\alpha}^i \hat{t}_k^i + \hat{\beta}^i \hat{s}_k^i, \tag{50}$$

where $\hat{\boldsymbol{t}}^i$ and $\hat{s}^i$ are the 'spines' defined on surface Γ_1 and Γ_2, respectively.

REFERENCES

1. M.A. Tehrani, S.H. Bitteston and P.J.G. Long. 'Flow instabilities during annular displacement of one non-Newtonian fluid by another', *Exp. Fluids*, **14**, 246–256 (1993).
2. A. Huerta and W.K. Liu, 'Viscous flow with large free surface motion', *Comput. Meth. Appl. Mech. Eng.*, **69**, 277–324 (1988).
3. T.J.R. Hughes, W.K. Liu and T.K. Zimmerman, 'Lagrangian–Eulerian finite element formulation for incompressible viscous flows', *Comput. Meth. Appl. Mech. Eng.*, **29**, 329–349 (1981).
4. A. Soulaimani, M. Fortin, G. Dhatt and Y. Ouellet, 'Finite element simulation of two- and three-dimensional free surface flows', *Comput. Meth. Appl. Mech. Eng.*, **86**, 265–296 (1991).
5. P. Szabo and O. Hassager, 'Simulation of free surfaces in 3D with the arbitrary Lagrange–Euler method', *Int. J. Numer. Methods Eng.*, **38**, 717–734 (1995).
6. P. Szabo and O. Hassager, 'Displacement of one Newtonian fluid by another: density effects in axial annular flow', *Int. J. Multiphase Flow*, **23**, 113–129 (1997).
7. S.F. Kistler and L.E. Scriven, 'Coating flows' in J.R.A Pearson and S.M. Richardson (eds.), *Computational Analysis of Polymer Processing*, Applied Science, Essex, 1983, pp. 243–299.
8. Bird, R.B., Armstrong, R.C. and Hassager O., *Dynamics of Polymeric Liquids*, Vol. I, 2nd edn., Wiley, New York, 1987.
9. H. Lamb, *Hydrodynamics*, 6th edn., Dover, New York, 1945.
10. A.N. Brooks and J.R. Hughes, 'Streamline upwind/Petrov–Galerkin formulations for convection dominated flows with particular emphasis on the incompressible Navier–Stokes equations', *Comput. Meth. Appl. Mech. Eng.*, **32**, 199–259 (1982).
11. J.R. Hughes, M. Mallet and A. Mizukami, 'A new finite element formulation for computational fluid dynamics: II. Beyond SUPG', *Comput. Meth. Appl. Mech. Eng.*, **54**, 341–355 (1986).
12. P. Henriksen. 'Simulation of ultrafiltration', *Ph.D. Thesis*, Technical University of Denmark, 1991.
13. O.C. Zienkiewicz and K. Morgan, *Finite Elements and Approximation*, Wiley-Interscience, New York, 1983.
14. F. Brezzi and M. Fortin, *Mixed and Hybrid Finite Element Methods*, Springer, New York, 1991.
15. K.J. Ruschak, 'A three-dimensional linear stability analysis for two-dimensional free boundary flows by the finite-element method', *Comput. Fluids*, **11**, 391–401 (1983).
16. P.J.G. Long. 'Experimental studies of fluid–fluid displacement in annuli', *Ph.D. Thesis*, Cambridge University, 1991.
17. P. Szabo, 'Simulation of multiphase flow', *Ph.D. Thesis*, Technical University of Denmark, 1994.
18. Donea, J., Giuliani, S. and Halleux, J.P., 'An arbitrary Lagrangian–Eulerian finite element method for transient dynamic fluid–structure interactions', *Comp. Meth. Appl. Mech. Eng.*, **33**, 689–723 (1982).
19. Flumerfelt, R.W., 'Laminar displacement of non-Newtonian fluids in parallel plate and narrow gap annular geometries', *SPE J.*, **April**, 169–180 (1975).
20. I.C. Walton, 'Displacement of two miscible fluids in a vertical channel', *Presented at the 31st British Theoretical Mechanics Colloquium*, Exeter, England, April 1989.
21. G.I. Taylor, 'Deposition of a viscous fluid on the wall of a tube', *J. Fluid Mech.*, **10**, 161–165 (1961).
22. O. Wambersie and M.J. Crochet, 'Transient finite element method for calculating steady state three-dimensional free surfaces', *Int. J. Numer. Methods Fluids*, **14**, 343–360 (1992).